This is a preprint, the final version is subject to change, of the American Mineralogist (MSA)
Cite as Authors (Year) Title. American Mineralogist, in press.
(DOI will not work until issue is live.) DOI: http://dx.doi.org/10.2138/am.2013.4300

Revision 1.1

The pressures and temperatures of meteorite impact: Evidence from micro-Raman mapping of mineral phases in the strongly shocked Taiban ordinary chondrite

Tayro E. Acosta-Maeda[1,2,*], Edward R. D. Scott[2], Shiv K. Sharma[2], and Anupam K. Misra[2]. [1]Department of Geology & Geophysics, University of Hawaii, Honolulu, HI 96822, USA [2]Hawaii Institute of Geophysics and Planetology, SOEST, University of Hawaii, Honolulu, HI 96822, USA.

*e-mail: tayro@hawaii.edu

Abstract

Taiban is a heavily shocked L6 chondrite showing opaque melt veins. Raman spectroscopy was used to characterize the high-pressure silicate assemblages in a thin section crossed by a shock created 4 mm wide melt vein. Raman spectra using different excitation wavelengths allowed identification of mineral phases such as olivine, wadsleyite, ringwoodite, high-Ca clinopyroxene, majorite-pyrope, jadeite, maskelynite and lingunite. Olivine is Fe depleted in contact with the ringwoodite, which suggests chemical fractionation during a solid-state olivine-ringwoodite transformation. Raman imaging revealed a close correlation between the blue ringwoodite color and the peak observed at 877 cm^{-1}; this signal shows strong near-resonance Raman enhancement when measured with near-IR excitation lines (785 and 830 nm) close to the optical absorption bands of the ringwoodite. We propose that the blue color of the ringwoodite is due to a small amount of iron in four-fold coordination inside the spinel structure, and that yields the observed spectral features in differently colored ringwoodite. Under the formation

conditions of the studied silicate pocket, all enstatite transformed to a majorite-pyrope solid solution, whereas the high-Ca clinopyroxene likely remained unchanged. Maskelynite grains in the margins of the pocket often contain lingunite or are totally transformed to jadeite. Based on static high-pressure results, the mineral assemblages in the pocket suggest peak pressure in the 17-20 GPa range with maximum temperature (T_{max}) in the range 1850-1900 K as the formation conditions for this Taiban chondrite during shock.

Keyword: micro-Raman, resonance Raman, ringwoodite, solid-state transformation; shock metamorphism

Introduction

High-pressure polymorphs of major minerals are commonly found in shocked meteorites. During the formation and later evolution of the Solar System (Raymond 2010; Wetherill 1980), asteroids repeatedly collided with each other and with larger bodies triggering shock waves. Meteorites that underwent such shock waves show different shock effects depending on the peak pressures and temperatures, and duration of the collision events (Stöffler et al. 1991).

Minerals commonly found in or near melt veins in highly shocked chondrites include: ringwoodite; majorite; wadsleyite; magnesiowüstite; akimotoite; lingunite; silicate–perovskite; and maskelynite (Chen et al. 1996; Chen and El Goresy 2000; Ferroir et al. 2008; Mori 1994; Price et al. 1983; Sharp et al. 1997; Tomioka and Fujino 1997; Xie et al. 2006). As the shock front triggered by a collision spreads through the irregularities of the rock, melt veins and shocked pockets form depending on pressure and temperature

This is a preprint, the final version is subject to change, of the American Mineralogist (MSA)
Cite as Authors (Year) Title. American Mineralogist, in press.
(DOI will not work until issue is live.) DOI: http://dx.doi.org/10.2138/am.2013.4300

conditions and the properties of the rock in each point. High-pressure phases form in these areas by solid-state transformations of the original minerals or fractional crystallization from the melt. Based on results from static high pressure and shock recovery experiments, the observed crystallization assemblages can aid in constraining the conditions of melt vein crystallization (Sharp and De Carli 2006). However, these methods present some difficulties. Shock recovery experiments probably produce lower temperatures and shorter shock durations than natural impacts. Similarly, equilibrium phase diagrams obtained from static high-pressure experiments fail to reproduce the large departures from equilibrium that mineral phases experience during shock. Furthermore static experiments do not produce direct transformation from low-pressure phases without forming intermediate structures (e.g., olivine to ringwoodite without forming wadsleyite) (Sharp and De Carli 2006; Stöffler et al. 1991; Xie and Sharp 2007; Xie et al. 2006).

Ringwoodite γ-$(Fe,Mg)_2Si0_4$ is the high-pressure polymorph of olivine with spinel structure. It is found as a rare mineral in shocked meteorites and arguably in impact craters by transformation from olivine, and is considered to be the major constituent of the lower part of the mantle transition zone (Binns et al. 1969; Ringwood 1975; Rull et al. 2007). Thus, the physical properties of the ringwoodite are key to understanding the behavior of that zone in the Earth's interior. The mineral has also been subject of abundant research since its discovery by Binns et al. (1969) in the Tenham meteorite (e.g., Gupta and Goyal 2011; Madon and Poirier 1983; Mosenfelder 2001; Price et al. 1982; Sinogeikin et al. 2003). Raman spectroscopy has been used extensively to assess the nature of the olivine polymorphs and other shock induced phases (e.g., Chen et al. 2007; Miyahara et al. 2008; Zhang et al. 2006). However, only a few studies have taken

advantage of the potential of Raman spectroscopy to provide compositional and structural information on the shock-induced ringwoodite phases (e.g., Feng et al. 2011).

Micro-Raman spectroscopy has successfully been used to provide univocal identification of minerals and glassy phases in meteorites as well as obtain additional information on structural and compositional variations inside mineral grains (Wang et al. 2001, 2004; Cooney et al. 1999). In combination with a microscope and an automated X-Y-Z stage, Micro-Raman spectroscopy can resolve sample sizes as small as 1 μm and place the data in its spatial context. Raman mapping, or Raman imaging, is a powerful technique that combines the mineralogical information included in the Raman spectra with spatial distribution, thus providing additional information on the petrography of the studied rocks and allowing for constraints on the crystallization histories (Fries et al. 2011; Frosch et al. 2007; Miyahara et al. 2008; Steele et al. 2007).

Sample

Taiban is a very strongly shocked, shock stage S6 ordinary L6 chondrite found in De Baca County, New Mexico, in 1975 (Lange D. E. et al. 1980). It shows multiple veins of opaque shock melt produced by shearing during the shock event that extracted the meteorite from its parent body. The melt veins form a network of complex branches surrounding pockets of highly shock altered, mosaicized, relict, or recrystallized silicates, and their high pressure polymorphs, along with droplets of immiscible troilite and metallic inclusions. Outside the melt vein, olivine presents only mosaicism with diapletic plagioclase glass (maskelynite) interstitial to olivine and the different pyroxenes (Scott et al. 2004; Stöffler et al. 1991). We studied the polished thin section UNM297 shown in Figure 1, which is intersected by a 4 mm wide melt vein in which the shock silicate

pockets are dominated by blue and white ringwoodite crystals that range in size from 10 to 100 μm. As ringwoodite is assembled in clasts within the vein and the surrounding white matrix, the high-pressure phase did not crystallize from the impact melt (Scott et al. 2004). Minor amounts of host olivine and the intermediate phase β-$(Mg,Fe)_2SiO_4$ wadsleyite also appear associated with the ringwoodite. The white matrix is composed mainly of different pyroxenes (high-Ca clinopyroxene and jadeite) and the high-pressure garnet polymorph of pyroxene, majorite. Plagioclase quenched to glass is conspicuous in the vicinity of the melt vein but was not found inside the lithic pockets or the melt areas; maskelynite grains present flow textures filling gaps between olivine and pyroxene. No lamellar intergrowth structures of ringwoodite and olivine were found so far in Taiban meteorite under optical microscope and SEM observations.

Methods

Raman spectroscopy with different excitation wavelengths was used in combination with optical images. Raman spectra were taken with three different instruments at the University of Hawai‘i. Spectra with 785 nm excitation wavelength were taken with a Kaiser Optical Systems' micro-Raman system. The system is composed of a 785 nm Invictus diode laser, a Leica microscope with imaging capabilities, a Kaiser Holospec spectrometer, and an Andor CCD camera. A 100 μm optical fiber transmits the laser light to the microscope and the Raman signal to the spectrometer. The laser is focused and the signal is observed through a 100X objective mounted on the microscope in backscattering geometry; the laser spot size on the sample was 2 μm. The system has a spectral range of 150-3300 cm^{-1}. Typical acquisition time was 150 s and laser output power was limited to 10 mW, after making sure no sample damage was induced at that power. In order to look

for resonance Raman effects and allow assessment of Raman peaks versus fluorescence peaks, additional spectra were taken with a Renishaw inVia micro-Raman system coupled with a 830 nm Invictus diode laser, a 244 nm frequency doubled Ar ion Lexus laser, and a 514.5 nm Ar ion laser. The microscope and spectrometer are coupled through optical mirrors and all the optics can be set to accommodate different wavelengths. The 514.5 and 830 nm lasers were focused on the sample through a 100X objective that also acted as a signal collector; laser spot sizes were approximately 2 μm for both wavelengths. Due to high absorption in the UV range, a 40X UV objective was used for the 244 nm line, which focuses the beam down to 5 μm spot size. Laser powers were kept under 5 mW for 830 nm, 1 mW for 514.5 nm, and 0.2 mW for 244 nm in order to avoid laser induced heating or sample photo-damage. Raman spectral ranges were 120-1600 cm^{-1} for 830 nm, and from 300-4000 cm^{-1} and 500-4000 cm^{-1} for 514.5 nm and 244 nm respectively.

Spectra with 532 nm excitation were collected using a WiTec Alpha300R confocal Raman microscope with a frequency doubled Nd-YAG laser (Coherent Compass) beam at 532 nm. The power of the 532 nm laser beam at the sample was 3 mW. All the spectra were acquired through a 100X objective with 300 s exposure time and a laser spot of around 2 μm. The Raman systems used for this study have a peak resolution of 6 cm^{-1} for the 514, 785, and 830 nm Raman systems, and 10 and 12 cm^{-1} for the UV 244 nm and 532 nm Raman systems, respectively (using the FWHM of the 1085 cm^{-1} calcite line measured with the various Raman systems). The mineral assemblages in the thin section of the Taiban meteorite were observed in transmitted, reflected, and cross-polarized light. Different areas were examined inside and outside the ~4 mm melt vein. The main focus

of the study was a silicate pocket inside the melt vein, surrounded by quenched glass. Outside the melt vein silicates present milder shock effects with the conspicuous presence of maskelynite.

For detection of minor phases, line and area scans were performed with the aid of an X-Y-Z stage with submicron accuracy in addition to point Raman measurements for 244, 785, and 830 nm. The sample was scanned under the laser beam in 2D for a Raman chemical image. Typically, step distances were chosen to match the 2 μm laser spot size and exposure times were set to 150 s. Data obtained during mapping runs were examined to locate the minor phases and obtain typical spectra for each phase and generate the Raman images. Typical images cover an area of approximately 600 μm^2 over 12x12 pixels and each phase was identified by its Raman signature peaks. Map intensity scales were generated by integrating the area or the peak height of each of the phases: the 856 cm^{-1} peak for olivine; 1013 cm^{-1} peak for high-Ca pyroxenes; 929 cm^{-1} peak for majorite; 799 cm^{-1} peak for ringwoodite; and 877 cm^{-1} peak for blue ringwoodite. Background subtraction and cosmic ray removal software processing was applied for each acquisition. Additional processing was needed to remove the small contribution of the microscope slide substrate and epoxy resin to the Raman signal. This was necessary for mineral phases transparent to the laser light at each wavelength. Representative spectra from the substrate were obtained at the edges of the slide and then subtracted from each of the spectra. Spectra operations and curve fittings were performed with the Grams/AI® 8.0 software package (Thermo Fisher Scientific, Inc.).

After the Raman measurements, the thin section was coated with carbon and studied with an electron microprobe (JEOL JXA-8500F) equipped with 5 tunable wavelength

dispersive spectrometers at the University of Hawai'i. Mineral chemical analyses were performed with a beam energy of 15 keV, a beam current of 15 nA and an electron beam diameter of typically 5 μm. A combination of natural and synthetic standards was used for the calibration. Oxygen was calculated by cation stoichiometry and included in the matrix correction. Typical detection limits were 0.010 weight percent for Al kα, 0.012 weight percent for P kα, 0.014 weight percent for Na kα, 0.019 weight percent for Ti kα, and 0.035 weight percent for Mn kα. The matrix correction method was ZAF or Phi-Rho-Z calculations and the mass absorption coefficients dataset was LINEMU.

Results and discussion

Raman spectra imaging and single point measurements were taken in and around the biggest ringwoodite crystal; the results from the mineral characterization are shown in Figure 2. Some additional spectra were recorded in other areas of the white matrix, other silicate pockets, and in several points in the mineral assemblages outside the melt vein.

Olivine, wadsleyite, and ringwoodite: Raman signature peaks of olivine are found at several points in and around the ringwoodite. The spectra of the grains within the ringwoodite and between grains show the characteristic peaks of olivine at 824 and 856 cm^{-1}, referred to as DB1 and DB2 bands, respectively (after Kuebler et al. 2006), in good agreement with the shifts found in forsterite (Chopelas 1991). This pair originates from the Si-O_{nb} bond stretching in the $[SiO_4]^{4-}$ tetrahedral and have a mixed character of υ_1 and υ_3 modes (Lam et al. 1990). An additional olivine peak appears at 962 cm^{-1} within the ringwoodite and in the olivine filling the 1 μm crack between the ringwoodite grains. Olivine and pyroxene-majorite assemblages or the melt vein are in direct contact with the

ringwoodite around the rest of the perimeter. According to a Raman composition calibration of olivine developed by Kuebler et al. (2006), olivine intermingled with the ringwoodite inside the lithic pocket in the melt vein is Fo_{88}, while olivine filling the 1 μm crack is Fo_{94}. In the host rock, olivine is Fo_{78} (Fig. 3, Tables 1 and 2).The olivine inside the pocket is intermingled with the ringwoodite formed after shock and found in small grains showing dendritic textures or filling the 1 μm crack between ringwoodite grains (Figs. 2 and 4). The discrepancy in the calculated Fo of the olivine located within the ringwoodite is most likely due to the difference in sampling depth between the two techniques and the Raman spectra of that area showing a contribution of both olivine with dendritic shapes and ringwoodite, thus inducing a bigger error in the estimation of the Raman peak positions. The olivine in the host rock is predominantly fine grained (however, crystals up to 100 μm are found in some areas) and is also found in inclusions and among high–Ca and low-Ca pyroxenes, and maskelynite.

Spectra taken in the inner points of the crystal show Raman fingerprints of pure ringwoodite. The vibrations located at 301, 589, 799 (referred to as RA1), and 844 cm^{-1} (referred to as RA2) correspond to ringwoodite, γ-$(Fe,Mg)_2Si0_4$. These vibrations have also been observed in natural ringwoodite lamellae in the Sixiangkou meteorite (Chen et al. 2007), NWA 1662 (Taran et al. 2009), and in synthetic ringwoodite (Akaogi et al. 1984; Chopelas et al. 1994; Kleppe et al. 2002a; McMillan and Akaogi 1987). The Raman mode at 844 cm^{-1} corresponds to pure Si-O bond stretching, A_{1g} symmetry. The signals found at 301, 589, and 799 cm^{-1} are T_{2g} modes, opposite oscillations of the two tetrahedral centers (Yu and Wentzcovitch 2006). RA1 and RA2 probably have a mixed character of υ_1 and υ_3 modes, similar to that observed for olivine doublet DB1 and DB2.

Additional measurements taken with excitation wavelengths, 244, 514.5, and 830 nm confirm that the peak observed at 877 cm^{-1} corresponds to the ringwoodite structure. The same peak was observed elsewhere and researchers have proposed that it is caused by the presence of a defect induced vibrational mode, to a inverse spinel structure in which the Mg and Fe ions are both in fourfold and sixfold coordination, or to the presence of glassy material (Kleppe et al. 2002b; Nagy et al. 2010a, 2010b). As shown in Figures 5 and 6, the intensity of the 877 cm^{-1} signal presents a remarkably accurate spatial correlation with the color observed by optical microscopy and polarized light. The intensity is higher when the ringwoodite is deep blue, intermediate in clear blue areas, and absent when the ringwoodite is colorless. This applies to at least five different ringwoodite grains of different and variable colors in different instruments, ruling out crystal orientation being the cause of the 877 cm^{-1} peak. The ringwoodite spectra also present twofold broadening of line widths in blue ringwoodite with a comparable 877 cm^{-1} peak contribution with respect to the lines RA1 and RA2. White ringwoodite, with a negligible 877 cm^{-1} contribution, shows a half width of 22 cm^{-1} for the RA1 peak, while blue ringwoodite shows an increased half width to 54 cm^{-1}.

The ringwoodite spectrum shows additional bands at 495 cm^{-1} and at a strong band at 225 cm^{-1} with a shoulder at 175 cm^{-1}. These bands (also observed by Sharp et al. 2009 and Taran et al. 2009 for blue ringwoodite) are not due to fluorescence because they are observed at the same Raman shift with 532, 785, and 830 nm laser excitation wavelengths. As in the observations of Sharp et al. (2009) and Taran et al. (2009), these bands appear only for blue ringwoodite when excited with a 532 nm laser; however they are observed for both clear and blue ringwoodite when exited with near-IR wavelengths

(785, and 830 nm), although less intense in the clear samples. These bands probably correspond to translational lattice modes in the ringwoodite structure because the positions are close to those measured for lattice modes of forsterite (Iishi 1978). Raman measurements also show that it is anhydrous ringwoodite, because no O-H modes have been detected under 244 or 514.5 nm excitation wavelengths. Minor amounts of wadsleyite are inferred from weak Raman peaks at 723 and 919 cm^{-1}, observable under 514.5 nm excitation (Chopelas 1991b; McMillan and Akaogi 1987).

Previous observations showed two different mechanisms for the transformation from olivine to its high-pressure polymorphs. Two mechanisms have been proposed for the crystallization of ringwoodite based on a solid-state transformation: incoherent nucleation on olivine grain boundaries; or coherent intracrystalline nucleation of ringwoodite (Chen et al. 2006; Kerschhofer et al. 1996, 1998, and 2000; Kubo et al. 2004; Ohtani et al. 2004; Putnis and Price 1979). More recent observations (Feng et al. 2011; Miyahara et al. 2008) suggest fractional crystallization of wadsleyite and ringwoodite from a melt of olivine composition. Ringwoodite in the Taiban meteorite contains minor amounts of wadsleyite and olivine depleted in Fe to different extents in the vicinity of the ringwoodite grains with respect to the host olivine (Fo_{78}–Fo_{94}, Tables 1 and 2). Thus, our results suggest that some chemical fractionation took place. The size, shape, and assemblages of the ringwoodite clasts in the pyroxene white matrix entrained in the melt vein and absence of wadsleyite crystals suggest a solid state transformation. Reflected light microphotography of the relict Fe-depleted olivine entrained in the bigger ringwoodite crystal shows darker olivine surrounded by ringwoodite due to the difference in light reflection coefficients between the two fractionated polymorphs (Fig. 4). The dendritic textures of the olivine

253 core are similar to those reported by Xie et al. (2012) in olivine cores inside ringwoodite
254 rims in GRV022321 and support the idea of a solid state transformation with diffusion
255 controlled growth between olivine and ringwoodite.

256 Ideally, the approximate composition of ringwoodite can be inferred from the Raman
257 peaks (Feng et al. 2011). The main peaks measured in the bulk of the ringwoodite grain
258 are two major vibrations located at 798.8 and 843.2 cm^{-1}. Near the boundaries of the
259 grain, the peaks are shifted to 797.5 and 843.5 cm^{-1} near the majorite, and to 798.7 and
260 844.3 cm^{-1} near the crack filed with olivine. This suggests slight differences in Fe and Mg
261 ions content. Pure anhydrous γ-$MgSiO_4$ forms clear colored crystals with vibrations at
262 796 (RA1) and 835 cm^{-1} (RA2) (Chopelas et al. 1994) while hydrous γ-$(Mg_{0.89}Fe_{0.11})SiO_4$
263 ~1.6 wt% H_2O is blue in color and the RA2 peak is shifted towards higher frequencies,
264 841 cm^{-1}. However, the position of the RA2 peak is not dependant on ringwoodite Fe-Mg
265 contents despite ranging from 835 to 849 cm^{-1} (Feng et al. 2011). The ringwoodite
266 studied in the Taiban meteorite would be equivalent to 72-78% Fo according to the
267 Raman calibration developed by Feng et al. (2011), however that calibration is not
268 reliable near pure Fo values and is not consistent with earlier measurements (Chopelas et
269 al. 1994; McMillan and Akaogi 1987). Nevertheless, the Raman calculated values in our
270 study fall within ±6% Fo when compared to the EPMA results shown in Table 2.

271 The Raman pattern observed in Taiban is close to those of the ringwoodite γ-
272 $(Mg_{0.8},Fe_{0.2})_2SiO_4$ in the Tenham meteorite, 799 and 845 cm^{-1} (Sato and Nakamura 2010),
273 and some of the ringwoodite in the lamellae of the Sixiangkou meteorite (22-24 wt%
274 FeO), 799 and 844 cm^{-1} (Chen et al. 2006). A possible explanation for this small shift
275 found in the natural ringwoodite in these meteorites could be the presence of residual

276 stress from the shock that triggered the transformation or the following relaxation.
277 Sazonova et al. (2006) measured shifts of the RA1 peak up to 814 cm^{-1} (814, 843; and
278 812, 846, in two different spectra) in ringwoodite containing Al up to 9 wt %, Ti up to 0.2
279 wt %, and K up to 1 wt % synthesized in a shock experiment from biotite. Thus, the
280 presence of some ions dissolved in the ringwoodite, namely Al, Ti, or K, could also affect
281 the position of the RA1 Raman line of ringwoodite. EPMA results show that the position
282 changes can also be due to slight variations on Ti, Cr, Mn and P in different points in the
283 ringwoodite.

284 The cause of the blue ringwoodite color has been discussed in the past but it still remains
285 mostly unknown. Lingemann and Stöffler (1998) and Price et al. (1979) observed glassy
286 material around ringwoodite crystals in blue colored aggregates. However, this glassy
287 material was not present in the colorless ringwoodite in the Sixiangkou meteorite (Chen
288 et al. 1996). Iron has been ruled out as the cause of the blue coloration because of the
289 absence of correlation between the ringwoodite color and the iron content (Coleman
290 1977; Lingemann and Stöffler 1998; Taran et al. 2009). Lingemann and Stöffler (1998)
291 proposed that the blue color is due to light scattering effect produced by the glassy
292 material, and Nagy et al. (2011) suggested that the color is due to scattering in grain
293 boundaries in submicron grains. However Taran et al. (2009) performed transmission
294 electron microscopy on two foils from a colorless to dark blue ringwoodite grain and
295 found no glassy phase in the colored areas.

296 The coloration of the ringwoodite in the Taiban meteorite varies gradually within the
297 mineral grains. Colorless areas coexist with blue to dark blue zones forming bubbly or
298 filament patterns inside otherwise completely homogeneous mineral grains. In our study

we found a relation between the Raman spectra and the coloration of the ringwoodite. We assume the 877 cm^{-1} peak has remained mostly unnoticed in previous Raman measurements (with the exception of Kleppe et al. 2002b and Nagy et al. 2010a and 2010b) because of the strong dependence of the Raman signal on the excitation wavelength. As shown in Figure 7, the 877 cm^{-1} peak is not observable with 244 nm laser excitation. The peak is weak with respect to RA1 and RA2 with the widely used Ar 514.5 nm laser line and comparable in intensity when excited with 785 or 830 nm laser wavelengths. We attribute this intensity dependence to near-resonance Raman enhancement in the blue ringwoodite. Absorption spectra from blue and dark blue natural ringwoodite from NWA 1662 and NWA 463 meteorites present a strong absorption line centered at 793 nm (Taran et al. 2009). Synthetic blue ringwoodite presents similar absorption bands due to its iron content (Keppler and Smith 2005). In natural samples, the absorption is stronger in darker colored grains and weaker in colorless ringwoodite. This absorption band remarkably follows the same color correlation as observed in the 877 cm^{-1} Raman peak and explains why the enhancement is only observed in colored ringwoodite. The color correlation of the absorption spectra and the Raman spectra suggest that the cause of the color lies in the crystal structure of the ringwoodite. The absorption line was assigned by Keppler and Smith 2005 and Taran et al. 2009 to the electronic spin allowed $^5T_{2g} \rightarrow {}^5E_g$ transition of $^{VI}Fe^{2+}$ split by the trigonal distortion or Jahn-Teller effect. Similar Raman enhancements have been observed for iron containing oxides and oxyhydroxides, for which near resonance Raman occurs with 636 nm excitation due to an absorption band located near 640 nm; this band is a result of the $^6A_1(^6S) \rightarrow {}^4T_2(^4G)$ ligand field transitions of octahedrally coordinated Fe^{3+} (Nieuwoudt et

al. 2011; Sherman and Waite 1985). Resonance Raman has also been confirmed in several spinel structured oxides (Kashyap et al. 2009; Koshizuka et al. 1975; Lutz et al. 1991). Furthermore, the presence of unassigned peaks in Raman spectra from spinels due to disorder is not uncommon. The appearance of a new band in the non silicate spinel $MgAl_2O_4$ after heating induced disorder has been described as a contribution to the Raman spectrum from cation disorder in the form of Al ion redistribution from octahedral to tetrahedral sites inside the spinel structure (Cynn et al. 1992, 1993). Thus, the peak we observed at 877 cm^{-1} is probably due to cation redistribution inside the spinel structure.

Taran et al. (2009) suggested an inverse spinel structure for the clear varieties of ringwoodite, based on the apparent different natures of the absorption spectra of blue and colorless varieties. In the inverse spinel all Fe^{2+} ions and probably part of the Mg are found in tetrahedral sites of the cubic close-packed structure, and Si cations would be displaced to the octahedral sites. However, the observed Raman shifts of RA1 and RA2 do not significantly differ between colorless and blue ringwoodite, suggesting that most of the Si is in fourfold coordination. This is consistent with nuclear magnetic resonance (Stebbins et al. 2009) and X-ray diffraction observations (Hazen et al. 1993). On the other hand, the observed increase in the linewidths of RA1 and RA2 indicate some degree of structural disorder in blue ringwoodite. Therefore, our data is consistent with the explanation that the gradation in color of the ringwoodite is due to a spinel structure ranging from normal to marginally inverse. Assuming such cation disorder and that the band at 844 cm^{-1} comes from Si-O bonds stretching in tetrahedral sites (Yu and Wentzcovitch 2006), we tentatively assign the 877 cm^{-1} Raman band to symmetric Fe-O stretching of a small amount of iron in fourfold coordination. Because of the resonance

Raman enhancement effect, we believe that we are able to detect low trace amounts of Fe^{+2} in tetrahedral sites. In the same structure, no Raman signal would be expected from Mg ions in four or sixfold coordination due to the highly ionic nature of the Mg-O bonding. This position is relatively close to the Raman shifts of 830-832 cm^{-1} reported for FeO_4 tetrahedra in $K_2[FeO_4]$ by Gonzalez-Vilchez and Griffith (1972). The difference of approximately 45 cm^{-1} with respect to the $\upsilon_1(A_1)$ band at 830 cm^{-1} could be due to contributions of the following: the coupling between SiO_4 and $^{IV}FeO_4$ tetrahedra; induced distortion by the SiO_6 octahedra; or a shorter Fe-O bonding length, consistent with the high pressure nature of the phase. Small bond distance differences can yield to large Raman shifts, e.g., in the transition between olivine and ringwoodite the increase of the Si-O distances of 0.02 ± 0.0005 Å (Hazen et al. 1993) induces a Raman shift of 10-25 cm^{-1} between the main peaks in olivine and ringwoodite. If the 877 cm^{-1} Raman band is produced indeed by Fe-O stretching, one would expect to also observe Fe-O bending modes and SiO_6 octahedral symmetrical stretching. The υ_2 and υ_4 modes of the FeO_4 tetrahedral are reported to be in the region of 300-400 cm^{-1} (Gonzalez-Vilchez and Griffith 1972) and could possibly be the unassigned, enhanced bands we observed in that region (Fig. 5). The spectra of the SiO_6 octahedral should resemble that of stishovite with two intense modes, A_{1g} at 753 cm^{-1} and B_{1g} at 231 cm^{-1} (Hemley et al. 1986). The band corresponding to the A_{1g} mode may be a shoulder of the RA1 ringwoodite band at 799 cm^{-1} (e.g., 765 cm^{-1}, Fig. 5). Similarly, the band assigned to the B_{1g} mode could possibly contribute to the broad set of bands centered at 225 cm^{-1}. The near-IR Raman enhancements of these bands (~231, 300-400, ~753, and 877 cm^{-1}) support these tentative assignments.

Pyroxenes and majorite. White grains show pyroxene Raman fingerprints **(**Fig. 8**)**. The high-Ca clinopyroxene (augite/diopside, *C*2/*c* monoclinic pyroxene) shows two intense peaks, the first one at 1013 cm^{-1} corresponding to the Si-O_{nb} bond stretching in the $[SiO_3]^{2-}$ unit of pyroxene chain, and the second peak at 667 cm^{-1} corresponding to the bridging oxygen stretch in the Si-O_{br}-Si bond of the $[Si_2O_6]^{4-}$ unit. Three smaller peaks are present in the range 300-400 cm^{-1}; 327, 369, and 395 cm^{-1} created by the displacements of cations from their equilibrium lattice positions or by or O-Si-O bending modes (Huang et al. 2000; Wang et al. 2001; Yang et al. 2009). A small amount of jadeite is also present in the white matrix. Jadeite has the ideal formula $NaAlSi_2O_6$ and shows three main characteristic signals at 698, 377, and 204 cm^{-1}. Similar to the high-Ca pyroxene, jadeite is a *C*2/*c* monoclinic pyroxene and the 698 cm^{-1} band originates from Si-O_{br}-Si vibrations within the silicate chains, and 377 and 304 cm^{-1} are likely lattice modes involving cation-O interactions or O-Si-O bending modes. Additional jadeite bands appear at 988, 1035 (Si-O stretching vibrations), and 756 cm^{-1} as well as other smaller bands in the range 200-600 cm^{-1} showing, respectively, cation vibrations and O-Si-O bending modes of SiO_4 tetrahedra (Huang et al. 2000; Wang et al. 2001; Yang et al. 2009).

Along with the pyroxene crystals, majorite assemblages are present in the white matrix. The most intense modes of majorite are found at 597 and 929 cm^{-1} (Rauch et al. 1996). Majorite is the cubic garnet polymorph of pyroxene. It has previously been found in the Coorara, Catherwood, Pampa del Infierno, Tenham, Sixiangkou, and Peace River chondritic meteorites (Smith and Mason 1970; Coleman 1977). Majorite forms in these meteorites from low-Ca pyroxenes (Chen and Xie 2008; Coleman 1977; Mao et al. 1982;

Smith and Mason 1970). Ca-rich majorite has been observed in the Shergotty and Yamato 75100 meteorites transformed from the host high-Ca pyroxene (Malavergne et al. 2001; Tomioka and Kimura 2003). The peak positions of majorite in the Taiban meteorite are in good agreement with the values provided by Rauch (1996) for pure $MgSiO_3$. The peak at 929 cm^{-1} is probably the A_{1g} mode from the symmetrical stretch of the SiO_4 group; and the 597 cm^{-1} has been assigned to the A_{1g} mode of the O-Si-O bending in the SiO_4 tetrahedral. However, there is a significant line width increase in several of the measured crystals, possibly due to some deformational stress in the crystals or a small contribution of pyrope in solid solution with the majorite (Hofmeister et al. 2004; Manghnani et al. 1998; McMillan et al. 1989). Jadeite Raman signals often appear in combination with diopside or majorite peaks, suggesting that jadeite mineral grains are smaller than the laser spot size in the mapped areas.

The pyroxene-majorite assemblages completely surround the ringwoodite crystals in the silicate pocket. These assemblages are mainly composed of high-Ca pyroxene, majorite, and jadeite. The presence of high-Ca pyroxene and majorite suggests that under the pressure and temperature conditions that the silicate pocket experienced, all the low-Ca pyroxene metamorphosed into the its high pressure phase majorite. The calcium pyroxene, however, reversed a high pressure transformation after the shock or remained unchanged. Similar assemblages were found in the Sixiangkou meteorite. Zhang et al. (2006) suggested that the preserved high-Ca pyroxene could be attributed to the higher temperature needed for the high-Ca pyroxene to transform to Ca-rich majorite, in combination with a very sluggish phase transformation rate. This is possibly due to the large radium cation Ca^{2+} (0.99 Å) in the crystal structure, whose coordination is more

414 difficult to modify under high pressures than that of Mg^{2+} (0.66 Å) and Fe^{2+} (0.74 Å) in
415 the low-Ca pyroxenes (Zhang et al. 2006). Jadeite probably formed from felsic
416 plagioclase feldspar after the pressures and temperatures experienced during shock.
417 Under pressure above the maskelynite stability field, plagioclase dissociates into jadeite
418 and SiO_2 (Liu 1978); jadeite has been found in other chondrites with similar compositions
419 as the plagioclase glass in the vicinity of melt veins (Ohtani et al. 2004). In the Taiban
420 meteorite pocket, the micron-sized jadeite crystals suggest that plagioclase melted and
421 dissociated into jadeite and SiO_2. The maskelynite in the host rock shows increasing
422 deformation and flow textures towards the melt vein, consistent with total melting inside,
423 where jadeite formed. The absence of the Raman signature peaks of SiO_2 polymorphs can
424 be explained if jadeite crystallizes from amorphous plagioclase while the crystallization
425 of stishovite is significantly delayed (Kubo et al. 2010), leaving the SiO_2 in form of glass.

426 *Maskelinite and lingunite*: Large amounts of plagioclase glass are found in the host rock
427 areas compared to the relict plagioclase glass located in the margins of the silicate pocket,
428 near the host rock. Plagioclase glass forms clear isotropic grains (Stöffler et al. 1991,
429 their Fig. 12). The spectra of both silicate glasses are shown in Figure 9. The spectrum is
430 dominated by a broad set of bands characteristic of plagioclase feldspar glass, centered
431 around 480 cm^{-1}. This is in good agreement with the spectra reported by Sharma et al.
432 (1983) for glass of anorthite composition and with earlier measurements of maskelynite
433 from natural samples (Chen and El Goresy 2000; Fritz et al. 2005). This band has been
434 attributed to the motion of the oxygen atom along a line bisecting the T-O-T angle (where
435 T = Si or Al) and is characteristic of the feldspar structure, which contains four-
436 membered rings of TO_4 tetrahedra (Sharma et al. 1983). The weak shoulder located

around 570 cm^{-1} has been assigned to three member rings of TO_4 tetrahedra in the framework glasses (Galeener and Geissberger 1983; Sharma et al. 1997). Its low intensity is consistent with the observations for highly shocked plagioclase (Fritz et al. 2005). The spectra of plagioclase glass in the high frequency range shows slightly different patterns when measured with different wavelengths. The Si-O stretch bands at 900-1100 cm^{-1} appear in the spectra recorded with 532 nm laser excitation. With 830 nm laser excitation a strong broad band appears at 990 cm^{-1} (904 nm). This band is probably due to rare earth elements fluorescence, likely Nd, whose strongest fluorescence band is also found around 907 nm. Lingunite, $(Na,Ca)AlSi_3O_8$, is one of the high-pressure polymorphs of plagioclase. It possesses hollandite structure and was first observed by Gillet et al. (2000) in the Sixiangkou chondrite. Lingunite Raman peaks appear along with the glass spectrum in the maskelynite grains inside the melt vein, at 210, 274, and 763 cm^{-1}. These peaks are characteristic of the hollandite structure: the signal at 763 cm^{-1} corresponds to SiO_6 octahedral symmetrical stretching; and the peaks at 210 and 274 cm^{-1} correspond to the splitting of the B_{1g} mode. A band resulting from the splitting of the B_{2g} mode appears at 973 cm^{-1} (Gillet et al. 2000; Liu et al. 2009). In Figure 9, the 973 cm^{-1} superimposes on the fluorescence feature around 990 cm^{-1}. It has been suggested that lingunite is formed by a solid-state transformation from plagioclase (Tomioka et al. 2000) or by crystallization from a melt (Gillet et al. 2000). Similarly, it has been suggested that plagioclase glass is a quenched melt as opposed to diaplectic glass, maskelynite (Chen and El Goresy 2000). The plagioclase glass grains in the studied thin slide of the Taiban meteorite present signs of ductile deformation but no evidence of extensive melting, either inside the melt vein or in the host rock. Furthermore, Raman bands of

460 recrystallized plagioclase were not observed in any of the measured grains. If the
461 plagioclase had melted we would expect some degree of recrystallization unless the
462 quenching rate was unrealistically fast (Fritz et al. 2005). Thus, plagioclase in the Taiban
463 meteorite seems to be diaplectic glass and the lingunite appears to be formed by a solid-
464 state transformation, as suggested by Kubo et al. (2010).

465 According to the results of static high-pressure melting experiments of the Allende
466 meteorite (Agee et al. 1995), the presence of crystals of ringwoodite, majorite, high-Ca
467 pyroxene and traces of wadsleyite can constrain the P-T formation conditions for the
468 studied silicate pocket to 17-20 GPa with a T_{max} in the range 1850-1900 K. The presence
469 of Fe-Ni droplets and a variety of sulfides in droplets and filling cracks is also consistent
470 with that P-T range. Our Raman and SEM observations in the studied area did not yield
471 signals corresponding to higher pressure phases such as magnesiowüstite or silicate
472 perovskite, thus the static pressure equivalent is probably below 20 GPa.

473 **Acknowledgements**

474 The authors would like to thank Zhidong Xie and another anonymous reviewer for the
475 helpful discussions and reviews; also Nancy Hulbirt, Brooks Bays and May Izumi for
476 their valuable help with figures and editing, and Eric Hellebrand for his invaluable help
477 with the EPMA measurements. This work was supported in part by NASA under a
478 MIDDP grant NNX07AV44G.

479 **References Cited**

480 Agee, C.B., Li, J., Shannon, M.C., and Circone, S. (1995) Pressure-temperature phase
481 diagram for the Allende meteorite. J. Geophys. Res., 100, 17725-17740.

482 Akaogi, M., Ross, L.N., McMillan, O., and Navrotsky, A. (1984) The Mg_2SiO_4
483 polymorphs (olivine, modified spinel and spinel) -thermodynamic properties from
484 oxide melt solution calorimetry, phase relations, and models of lattice vibrations.
485 American Mineralogist, 69, 499-512.
486 Binns R.A., Davis, R.J., and Reed, S.J.B. (1969) Ringwoodite, natural $(Mg,Fe)_2SiO_4$
487 spinel in the Tenham meteorite. Nature 221, 943-944.
488 Chen M., and El Goresy, A. (2000) The nature of maskelynite in shocked meteorites: Not
489 a diaplectic glass but a glass quenched from shock-induced dense melt at high
490 pressures. Earth and Planetary Science Letters, 179, 489-502.
491 Chen, M., and Xie, X. (2008) Two distinct assemblages of high-pressure liquidus phases
492 in shock veins of the Sixiangkou meteorite. Meteoritics and Planetary Science, 43,
493 823-828.
494 Chen, M., Sharp, T.G., El Goresy, A., Wopenka, B., and Xie, X. (1996) The Majorite-
495 Pyrope + Magnesiowüstite Assemblage: Constraints on the History of Shock Veins
496 in Chondrites. Science, 271, 1570-1573.
497 Chen, M., Li, H., El Goresy, A., Liu, J., and Xie, X. (2006) Fracture-related
498 intracrystalline transformation of olivine to ringwoodite in the shocked Sixiangkou
499 meteorite. Meteoritics and Planetary Science, 41, 731-737.
500 Chen, M., Chen, J., Xie, X., and Xu J. (2007) A microstructural investigation of natural
501 lamellar ringwoodite in olivine of the shocked Sixiangkou chondrite. Earth and
502 Planetary Science Letters, 264, 277-283.
503 Chopelas, A. (1991) Single crystal Raman spectra of forsterite, fayalite, and monticellite.
504 American Mineralogist, 76, 1101-1109.

505 Chopelas, A. (1991b) Thermal properties of β-Mg_2SiO_4 at mantle pressures derived from
506 vibrational spectroscopy: Implications for the mantle at 400 km depth, Journal of
507 Geophysical Research, 96, 11,817-11,829.
508 Chopelas, A., Boehler, R., and Ko, T. (1994) Thermodynamics and behavior of c-
509 Mg_2SiO_4 at high pressure: implications for Mg_2SiO_4 phase equilibrium. Physics and
510 Chemistry of Minerals, 21, 351-359.
511 Coleman, L.C. (1977) Ringwoodite and majorite in the Catherwood meteorite. Canadian
512 Mineralogist, 15, 97-101.
513 Cooney, T.F., Scott, E.R.D., Krot, A.N., Sharma, S.K., and Yamaguchi, A. (1999)
514 Vibrational Spectroscopic Study of Minerals in the Martian Meteorite ALH84001.
515 American Mineralogist, 84, 1569-1576.
516 Cynn, H., Sharma, S.K., Cooney, T.F., and Nicol, M. (1992) High-temperature Raman
517 investigation of order-disorder behavior in the $MgAl_2O_4$ spinel. Physical Review
518 B, 45, 500-502.
519 Cynn, H., Anderson, O.L., and Nicol, M. (1993) Effects of cation disordering in a natural
520 $MgAl_2O_4$spinel observed by rectangular parallelepiped ultrasonic resonance and
521 Raman measurements. Pure and Applied Geophysics, 141, 415-444.
522 Feng, L., Lin, Y., Hu, S., Xu, L., and Miao B. (2011) Estimating compositions of natural
523 ringwoodite in the heavily shocked Grove Mountains 052049 meteorite from
524 Raman spectra. American Mineralogist, 96, 1480-1489.
525 Ferroir, T., Beck, P., Van de Moortèle, B., Bohn, M., Reynard, B., Simionovici, A., El
526 Goresy, A., and Gillet, P. (2008) Akimotoite in the Tenham meteorite: Crystal

527 chemistry and high-pressure transformation mechanisms. Earth and Planetary
528 Science Letters, 275, 26-31.
529 Fries, M., Sellar, G., Allwood, A., and Bhartia, R. (2011) Raman in a Combined
530 Instrument Package: Co-Registered and "Smart Raman" Techniques. CORALS II
531 Abstract#4087.
532 Fritz, J., Greshake, A. and Stöffler, D. (2005) Micro-Raman spectroscopy of plagioclase
533 and maskelynite in Martian meteorites: Evidence of progressive shock
534 metamorphism. Antarctic Meteorite Research, 18, 96-116.
535 Frosch, T., Tarcea, N., Schmitt, M., Thiele, H., Langenhorst, F., and Popp, J. (2007) UV
536 Raman Imaging-A Promising Tool for Astrobiology: Comparative Raman Studies
537 with Different Excitation Wavelengths on SNC Martian Meteorites. Analytical
538 Chemistry, 79, 1101-1108.
539 Galeener, F.L., and Geissberger, A.E. (1983) Vibrational dynamics in ^{30}Si-substituted
540 vitreous SiO_2. Physical Review B, 27, 6199-6204.
541 Gillet, P., Chen, M., Dubrovinsky, L., and El Goresy, A. (2000) Natural $NaAlSi_3O_8$-
542 hollandite in the shocked Sixiangkou meteorite. Science, 287, 1633-1636.
543 Gonzalez-Vilchez, F., and Griffith, W.P. (1972) Transition-metal tetra-oxo-complexes
544 and their vibrational spectra. Journal of the Chemical Society, Dalton
545 Transactions 1416-1421.
546 Gupta, S., and Goyal, S.C. (2011) Equation of State for Mg_2SiO_4 (α-forsterite, β-
547 wadsleyite and γ-ringwoodite): ab-Initio. AIP Conference Proceedings 1349, 200-
548 201.

549 Hazen, R.M., Downs, R.T., Finger, L.W., and Ko, J. (1993) Crystal chemistry of
550 ferromagnesian silicate spinels; evidence for Mg-Si disorder. American
551 Mineralogist, 78, 1320-1323.
552 Hemley, R.J., Mao, H.K., and Chao, E.C.T. (1986) Raman spectrum of natural and
553 synthetic stishovite. Physics and Chemistry of Minerals, 13, 285-290.
554 Hofmeister, A.M., Giesting, P.A., Wopenka, B., Gwanmesia, G.D., and Jolliff, B.L.
555 (2004) Vibrational spectroscopy of pyrope-majorite garnets: Structural
556 implications. American Mineralogist, 89, 132-146.
557 Huang, E., Chen, C.H., Huang, T., Lin, E.H., and Xu, J.-A. (2000) Raman spectroscopic
558 characteristics of Mg-Fe-Ca pyroxenes. American Mineralogist, 85, 473-479.
559 Iishi, K. (1978) Lattice dynamics of forsterite. American mineralogist, 63, 1198-1208.
560 Kashyap, S.C., Bhatti, K.P., Chaudhary, S., Pandya, D.K., and Sharma, S.K. (2009)
561 Chemically Synthesized Ferromagnetic $Zn_{1-x}Co_xO$ Nanocrystals: Raman
562 Investigations. Synthesis and Reactivity in Inorganic, Metal-Organic, and Nano-
563 Metal Chemistry, 39, 216-220.
564 Keppler, H., and Smyth, J.R. (2005) Optical and near infrared spectra of ringwoodite to
565 21.5 GPa: Implications for radiative heat transport in the mantle. American
566 Mineralogist, 90, 1209-1212.
567 Kerschhofer L, Sharp T.G., Rubie D.C. (1996) Intracrystalline transformation of olivine
568 to wadsleyite and ringwoodite under subduction zone conditions. Science, 274, 79-
569 81.
570 Kerschhofer, L., Dupas, C., Liu, M., Sharp, T.G., Durham, W.B., and Rubie, D.C. (1998)
571 Polymorphic transformations between olivine, wadsleyite and ringwoodite:

572 Mechanisms of intracrystalline nucleation and the role of elastic strain.
573 Mineralogical Magazine, 62, 617-638.
574 Kerschhofer, L., Rubie, D.C., Sharp, T.G., McConnell, J.D.C., and Dupas-Bruzek, C.
575 (2000) Kinetics of intracrystalline olivine-ringwoodite transformation. Physics of the
576 Earth and Planetary Interiors, 121, 59-76.
577 Kleppe, A.K., Jephcoat, A.P., and Smyth, J. R. (2002a) Raman spectroscopic study of
578 hydrous γ-Mg_2SiO_4 to 56.5 GPa. Physics and Chemistry of Minerals, 29, 473-476.
579 Kleppe, A.K., Jephcoat, A.P., Smyth J.R., Frost, D.J. (2002b) On protons, iron and the
580 high-pressure behavior of ringwoodite. Geophysical Research Letters, 29, 2021, 4
581 pages.
582 Koshizuka, N., Yokoyama, Y., Hiruma, H., and Tsushima, T. (1975) Resonance Raman
583 scattering in $CdIn_2S_4$. Solid State Communications, 16, 1011-1014.
584 Kubo, T., Ohtani, E., and Funakoshi, K. (2004) Nucleation and growth kinetics of the α-β
585 transformation in Mg_2SiO_4 determined by in situ synchrotron powder X-ray
586 diffraction. American Mineralogist, 89, 285-293.
587 Kubo, T., Kimura, M., Kato, T., Nishi, M., Tominaga, A., Kikegawa, T., and Funakoshi,
588 K. (2010) Plagioclase breakdown as an indicator for shock conditions of meteorites.
589 Nature Geoscience, 3, 41-45.
590 Kuebler, K.E., Jolliff, B.L., Wang, A., Haskin, L.A. (2006) Extracting olivine (Fo-Fa)
591 compositions from Raman spectral peak positions. Geochimica et Cosmochimica
592 Acta, 70, 6201-6222.

593 Lange D. E., Keil, K., and LaPaz, L. (1980) Catalog of the meteorite collection of the
594 Institute of Meteoritics at the University of New Mexico. Special Publication 21,
595 UNM Institute of Meteoritics.
596 Lam, P.K., Yu, R., LEE, M.W., Sharma, S.K. (1990) Structural distortions and
597 vibrational modes in Mg_2SiO_4. American Mineralogist, 75, 109-119.
598 Lingemann C. M., and Stöffler, D. (1998) New evidence for the colouration and
599 formation of ringwoodite in severely shocked chondrites. Lunar and Planetary
600 Science Conference XXIX, abstract #1308.
601 Liu, L.G. (1978) High-pressure phase transformation of albite, jadeite and nepheline.
602 Earth and Planetary Science Letters, 37, 438-444.
603 Liu, L., Lin, C.C., Yung, Y., Mernagh, T., and Irifune, T. (2009) Raman spectroscopic
604 study of K-lingunite at various pressures and temperatures. Physics and
605 Chemistry of Minerals, 36, 143-149.
606 Lutz, H.D., Müller, B., and Steiner, H.J. (1991) Lattice vibration spectra. LIX. Single
607 crystal infrared and Raman studies of spinel type oxides. Journal of Solid State
608 Chemistry, 90, 54-60.
609 Madon M. and Poirier J.P. (1983) Transmission electron microscope observation of α, β,
610 γ $(Mg,Fe)_2SiO_4$ in shocked meteorites: Planar defects and polymorphic transitions.
611 Phys. Earth. Planetary Interiors, 33, 31-44.
612 Manghnani, M.H., Vijayakumar, V., and Bass, J.D. (1998) High-pressure Raman
613 scattering study of majorite-garnet solid solutions in the system $Mg_4Si_4O_{12}$-
614 $Mg_3Al_2Si_3O_{12}$. In M.H. Manghnani and T. Yagi, Eds., Properties of Earth and

615 Planetary Materials at High Pressure and Temperature, 129-137. American
616 Geophysical Union, Washington, D.C.
617 Mao, H.K., Bell, P.M., and Boctor, N.Z. (1982) The mineral chemistry of majorite in L6
618 chondrites. Carnegie Institute Washington Yearbook 1981, 279-281.
619 McMillan, P., and Akaogi, M. (1987) Raman spectra of β-Mg_2SiO_4 (modified spinel) and
620 γ-Mg_2SiO_4 (spinel). American Mineralogist, 72, 361-364.
621 McMillan, P., Akaogi, M., Ohtani, E., Williams, Q., Nieman, R., and Sato, R. (1989)
622 Cation disorder in garnets along the $Mg_3Al_2Si_3O_{12}$-$Mg_4Si_4O_{12}$ join: an infrared,
623 Raman and NMR study. Physics and Chemistry of Minerals, 16, 428-435.
624 Miyahara, M., El Goresy, A., Ohtani, E., Nagase, T., Nishijima, M., Vashaei, Z., Ferroir,
625 T., Gillet, P., Dubrovinsky, L., and Simionovici, A. (2008) Evidence for fractional
626 crystallization of wadsleyite and ringwoodite from olivine melts in chondrules
627 entrained in shock-melt veins. Proceedings of the National Academy of Sciences,
628 105, 8542-8547.
629 Mori, H. (1994) Shock-induced phase transformations on the Earth and planetary
630 materials. Journal of the Mineralogical Society of Japan, 23, 171-178.
631 Mosenfelder, J. (2001) Experimental constrains on the depth of olivine metastability in
632 subducting lithosphere. Physics of the Earth and Planetary Interiors, 127, 165-180.
633 Nagy S., Józsa, S., Bérczi, S., Gucsik, A., Koós, M., and Veres, M. (2010a) Shock
634 induced high-pressure phases in the shock veins of NWA 5011 L6 chondrite. The
635 33rd Symposium on Antarctic Meteorites, June 8 and 9, 2010, National Institute of
636 Polar Research, Tachikawa City, Tokyo, Japan.

637 Nagy, S., Bérczi, S., Józsa, S., Gucsik, A., and Veres, M. (2010b) Olivine and pyroxene
638 high-pressure polymorphs in melt veins of the strongly shocked NWA 5011
639 meteorite sample. Lunar and Planetary Science Conference XLI, abstract #1228.
640 Nagy, S., Gyollai, I., Józsa, S., and Bérczi, S. (2011) Observation of colouration of
641 ringwoodite in the NWA 5011 L5-6 Chondrite. Lunar and Planetary Science
642 Conference XLII, abstract #1285.
643 Nieuwoudt, M.K., Comins, J.D., and Cukrowski, I. (2011) The growth of the passive film
644 on iron in 0.05 M NaOH studied in situ by Raman micro-spectroscopy and
645 electrochemical polarisation. Part I: near-resonance enhancement of the Raman
646 spectra of iron oxide and oxyhydroxide compounds. Journal of Raman Spectroscopy,
647 42, 1335-1339.
648 Ohtani, E., Kimura, Y., Kimura, M., Takata, T., Kondo, T., Kubo, T. (2004) Formation of
649 high-pressure minerals in shocked L6 chondrite Yamato 791384: constraints on
650 shock conditions and parent body size. Earth and Planetary Science Letters, 227,
651 505-515,
652 Price, G.D., Putnis, A., and Agrell, S.O. (1979) Electron petrography of shock-produced
653 veins in the Tenham chondrite. Contributions to Mineralogy and Petrology, 71, 211-
654 218.
655 Price, G.D., Putnis A., and Smith D.G.W. (1982) A spinel to γ-phase transformation
656 mechanism in $(Mg,Fe)_2SiO_4$. Nature, 296, 729-731.
657 Price, G.D., Putnis, A., Agrell, S. O., and Smith, D.G.W. (1983) Wadsleyite, natural β-
658 $(Mg, Fe)_2SiO_4$ from the Peace River meteorite. Canadian Mineralogist, 21, 29-35.

659 Putnis, A, and Price G.D. (1979) High-pressure (Mg, Fe)$_2SiO_4$ phases in the Tenham
660 chondritic meteorite. Nature, 280, 217-218.
661 Rauch, M., Keppler, H., Hafner, W., Poe, B., and Wokaun, A. (1996) A pressure-induced
662 phase transition in $MgSi0_3$-rich garnet revealed by Raman spectroscopy. American
663 Mineralogist, 81, 1289-1292.
664 Raymond, S.N. (2010) Formation of Terrestrial Planets. In R. Barnes, Eds. Formation
665 and Evolution of Exoplanets, Chapter 6, Wiley-VCH Verlag GmbH & Co. KGaA,
666 Weinheim, Germany. ISBN: 978-3-527-40896-2.
667 Ringwood, A.E. (1975) Composition and Petrology of the Earth's Mantle. McGraw-Hill,
668 London, New York, and Sydney, 1975. ISBN: 978-0-07-052932-8.
669 Rull, F., Martinez-Frias, J., and Rodríguez-Losada, J.A. (2007) Micro-Raman
670 spectroscopic study of El Gasco pumice, western Spain. Journal of Raman
671 Spectroscopy, 38, 239-244.
672 Sato, Y., and Nakamura, N. (2010) Shock melt veins of Tenham chondrite as a possible
673 paleomagnetic recorder: Rock magnetism and high-pressure minerals. Geochem.
674 Geophys. Geosyst., 11, Q04Z16.
675 Sazonova, L., Fel'dman, V., Kozlov, E., Dubrovinskaya, N., and Dubrovinskii, L. (2006)
676 Genesis of ringwoodite during metamorphism induced by impact waves:
677 Experimental data. Geochemistry International, 44, 137-142.
678 Scott, E.R., Sharma, K.S., and Chio, C.H. (2004) Micro-Raman and petrologic study of
679 shock-induced high-pressure minerals in the Taiban meteorite. GEORAMAN 2004:
680 6th International Conference on Raman spectroscopy Applied to the Earth and
681 Planetary Sciences, Honolulu, Hawaii, USA. June 6-11, 2004, 61-62.

682 Sharma, S.K., Simons, B., and Yoder, H.S. (1983) Raman study of anorthite, calcium
683 Tschermak's pyroxene, and gehlenite in crystalline and glassy states. American
684 Mineralogist, 68, 1113-1125.
685 Sharma, S.K., Cooney, T.F., Wang, Z., and van der Laan, S. (1997) Raman band
686 assignments of silicate and germanate glasses using high-pressure and high-
687 temperature spectral data. Journal of Raman Spectroscopy, 28, 697-709.
688 Sharp, T.G., and De Carli, P.S. (2006) Shock Effects in Meteorites. Meteorites and the
689 Early Solar System II, D. S. Lauretta and H. Y. McSween Jr. (eds.), University of
690 Arizona Press, Tucson, 653-677.
691 Sharp, T.G., Lingemann C.M., Dupas, C., and Stöffler D. (1997) Natural occurrence of
692 $MgSiO_3$-ilmenite and evidence for $MgSiO_3$-perovskite in a shocked L chondrite.
693 Science, 277, 352-355.
694 Sharp, T.G., Trickey, R., Xie, Z., and Decarli, P.S. (2009) Ringwoodite microstructures
695 in L-chondrites RC106 and Acfer 040: implications for transformation mechanisms.
696 Lunar and Planetary Science Conference XL, abstract #2541.
697 Sherman, D.M., and Waite T.D. (1985) Electronic spectra of Fe^{3+} oxides and oxide
698 hydroxides in the near IR to near UV. American Mineralogist, 70, 1262-1269.
699 Sinogeikin, S.V., Bass, J.D., and Katsura, T. (2003) Single-crystal elasticity of
700 ringwoodite to high pressures and high temperatures: implications for 520 km
701 seismic discontinuity. Physics of the Earth and Planetary Interiors, 36, 41-66.
702 Smith, J.V., and Mason, B. (1970) Pyroxene-garnet transformation in Coorara meteorite.
703 Science, 168, 832-833.

704 Stebbins, J.F., Smyth, J.R., Panero, W.R., and Frost, D.J. (2009) Forsterite, hydrous and
705 anhydrous wadsleyite and ringwoodite (Mg_2SiO_4): ^{29}Si NMR results for chemical
706 shift anisotropy, spin-lattice relaxation, and mechanism of hydration. American
707 Mineralogist, 94, 905-915.
708 Steele, A., Fries, M. D., Amudsen, H.E.F., Mysen B.O., Fogel, M.L., Schweizer, M., and
709 Boctor, N.Z. (2007) Comprehensive imaging and Raman spectroscopy of carbonate
710 globules from Martian meteorite ALH 84001 and a terrestrial analogue from
711 Svalbard. Meteoritics & Planetary Science 42, 1549-1566.
712 Stöffler, D., Keil, K., and Scott, E.R.D. (1991) Shock metamorphism of ordinary
713 chondrites. Geochimica et Cosmochimica Acta, 55, 3845-3897.
714 Taran, M., Koch-Müller, M., Wirth, R., Abs-Wurmbach, I., Rhede, D., and Greshake, A.
715 (2009) Spectroscopic studies of synthetic and natural ringwoodite, γ-$(Mg, Fe)_2SiO_4$.
716 Physics and Chemistry of Minerals, 36, 217-232.
717 Tomioka, N., and Fujino, K. (1997) Natural $(Mg,Fe)SiO_3$-Ilmenite and -Perovskite in the
718 Tenham Meteorite. Science, 277, 1084-1086.
719 Tomioka, N., and Kimura, M. (2003) The breakdown of diopside to Ca-rich majorite and
720 glass in a shocked H chondrite. Earth and Planetary Science Letters, 208, 271-278.
721 Tomioka, N., Mori, H., and Fujino, K. (2000) Shock-induced transition of $NaAlSi_3O_8$
722 feldspar into a hollandite structure in a L6 chondrite. Geophysical Research Letters,
723 27, 3997-4000.
724 Malavergne, V., Guyot, F., Benzerara, K., and Martinez, I. (2001) Description of new
725 shock-induced phases in the Shergotty, Zagami, Nakhla and Chassigny meteorites.
726 Meteoritics & Planetary Science, 36, 1297-1305.

727 Wang, A., Jolliff, B.L, Haskin, L.A., Kuebler, K.E., and Viskupic, K.M. (2001)
728 Characterization and comparison of structural and compositional features of
729 planetary quadrilateral pyroxenes by Raman spectroscopy. American Mineralogist,
730 86, 790-806.
731 Wang, A., Kuebler, K.E., Joliff, B.L., and Haskin, L.A. (2004) Raman spectroscopy of
732 Fe-Ti-Cr-oxides, case study: Martian meteorite EETA79001. American
733 Mineralogist, 89, 665-680.
734 Wetherill, G.W. (1980) Formation of the terrestrial planets. Annual Review of
735 Astronomy and Astrophysics, 18, 77-113.
736 Xie, Z., and Sharp, T.G. (2007) Host rock solid-state transformation in a shock-induced
737 melt vein of Tenham L6 chondrite. Earth and Planetary Science Letters, 254, 433-
738 445.
739 Xie, Z., Sharp, T.G., and DeCarli, P.S. (2006) High pressure phases in a shock-induced
740 melt vein of Tenham L6 Chondrite: constraints on shock pressure and duration,
741 Geochimica and Cosmochimica Acta, 70, 504-515.
742 Xie, Z., Li, X., Sharp, T.G., and De Carli, P.S. (2012) Shock-induced ringwoodite rims
743 around olivine fragments in melt vein of Antarctic chondrite GRV022321 :
744 Transformation Mechanism. Lunar and Planetary Science Conference XLIII,
745 abstract #2776.
746 Yang, H., Konzett, J., Frost, D. J., and Downs, R. T. (2009) X-ray diffraction and Raman
747 spectroscopic study of clinopyroxenes with six-coordinated Si in the
748 $(Mg_{0.5}Si_{0.5})Si_2O_6$-$NaAlSi_2O_6$ system. American Mineralogist, 94, 942-949.

749 Yu, Y. G., and Wentzcovitch, R. M. (2006) Density functional study of vibrational and
750 thermodynamic properties of ringwoodite. Journal of Geophysical Research, 111,
751 B12202.
752 Zhang, A., Hsu, W., Wang, R., and Ding, M. (2006) Pyroxene polymorphs in melt veins
753 of the heavily shocked Sixiangkou L6 chondrite. European Journal Mineralogy, 18,
754 719-726.
755

Figure captions

Figure 1. (a) Transmitted light photomicrograph of the black melt vein of the Taiban meteorite. Pockets inside the vein contain pyroxene (px) assemblages, blue and white ringwoodite grains (rgt), and relict plagioclase glass (pl). Ringwoodite tends to be clearer in color towards the mid section of the vein, approximately in the bottom right corner of this image. Black areas contain metal-sulfides, iron oxides, and metal inclusions, among other submicron phases. The host rock is mainly composed of assemblages of olivine, enstatite, high-Ca pyroxene, and plagioclase totally transformed to maskelynite. (b) Backscattered electrons image of the silicate pocket located in the center of the above image.

Figure 2. (a) Raman maps and phase distributions inferred from additional 2-D maps, 1-D lines, and single point measurements around the studied ringwoodite crystal. The ringwoodite is surrounded by pyroxenes and majorite assemblages. High-Ca pyroxene appears both alone and with jadeite in the Raman spectra of this area. Fe-depleted olivine is present in minor grains at the boundaries of the ringwoodite grain (Fo_{88}) and along the 1 μm crack separating the ringwoodite grains in the center and in the bottom of this image (Fo_{94}). (b) Backscattered electrons image of the same area. Olivine appears darker than the ringwoodite and pyroxene crystals. White dots show EMPA measurement points. The clear circle in the ringwoodite is due to damage of the carbon coating by the electron beam.

Figure 3. Olivine inside the pocket in the melt vein (a) and in the host rock (b) a few millimeters away from the melt vein in the same microscope slide. The olivine inside the pocket is intermingled with the ringwoodite formed after shock. The olivine in the host

779 rock is fine grained and found among pyroxenes. Raman lines are shifted up inside the
780 melt vein indicating a higher Fo content than the host olivine.

781 Figure 4. Olivine showing dendritic textures intermingled with the ringwoodite
782 grain. Inset shows the same area in backscattered electrons image; scale bar is 10 μm.

783 Figure 5. Raman spectra of (a) colorless and (b) deep blue ringwoodite. The intensity
784 of the 877 cm^{-1} peak is enhanced in the blue ringwoodite due to the resonance Raman
785 Effect with excitation at 785 nm. Several new bands also appear in the low frequency
786 region for deep blue ringwoodite. 785 nm laser excitation, 10 mW power output, 150 s
787 acquisition time. (c) Curve-fitting result for the spectrum of deep blue ringwoodite with
788 Lorentz-Gauss curve shapes. 830 nm laser excitation, 5 mW power output, 300 s
789 acquisition time.

790 Figure 6. Composition of Raman images showing the intensity of the 877 cm^{-1} peak
791 in the ringwoodite grain. The peak is more intense in the red areas, showing the close
792 correlation between the intensity of the peak and the blue ringwoodite color. The
793 arbitrary color scale shows the integrated area of the peak between 860 and 900 cm^{-1}.

794 Figure 7. Variation in the relative intensity of the peaks RA1, RA2, and 877 cm^{-1} in
795 blue ringwoodite far from grain boundaries with various laser excitation wavelengths due
796 to resonance Raman Effect. Excitation wavelength, laser power, and acquisition time are
797 (a) 244 nm, 0.5 mW and 1800 s (b) 514.5 nm, 1 mW, and 600 s (c) 785 nm, 10 mW, and
798 150 s, and (d) 830 nm, 5 mW, and 300 s, respectively.

799 Figure 8. Raman spectra of pyroxenes and majorite (mjt) in the white matrix of the
800 lithic pocket. Pyroxenes are High-Ca pyroxene (cpx) and jadeite (jad). High-Ca

pyroxene: 785 nm laser; 10 mW power output; 150 s acquisition time. Jadeite: 830 nm laser; 5 mW power output; 150 s acquisition time. Majorite: 532 laser; 3 mW power output; 300 s acquisition time.

Figure 9. Raman of plagioclase glass in the studied lithic pocket (A) and in the host rock (B) of the Taiban meteorite. Inside the melt vein (A), lingunite peaks appear along with the plagioclase glass Raman spectrum. Plots (a) and (b) show the spectrum of maskelynite inside the pocket (A); and (c) and (d) show the spectrum of maskelynite in the host rock (B). (a) 830 nm laser, 3 mW power output, 400 s acquisition time. (b) 532 nm laser, 3 mW power output, 300 s acquisition time. (c) 830 nm laser, 5 mW power output, 150 s acquisition time. (d) 532 nm laser, 3 mW power output, 300 s acquisition time. With 785 nm laser excitation spectrum was obscured by strong luminescence background.

814

815 **Appendix 1**. Sample. The meteorite used for this study is the Taiban (b), L6-S6 ordinary
816 chondrite. It was found in De Baca County, New Mexico in 1975 (Taiban (b) of
817 Lange D. E., et al. 1980, Catalog of the meteorite collection of the Institute of
818 Meteoritics at the University of New Mexico. Special Publication 21, UNM Institute
819 of Meteoritics.). Thin slides of the same meteorite were used in the work of Stöffler
820 et al. (1991). This is not the Taiban (b) LL6 ordinary chondrite found in the same
821 area in 1984 (Jeffrey N. Grossman, Meteoritical Bulletin 84, 2000), nor the Taiban
822 meteorite found in 1934 (Grady, M. M. (2001) Catalogue of Meteorites, 5th Ed.
823 Natural History Museum (London, England) Cambridge University Press). A new
824 name must be assigned to the Taiban (b) meteorite used in this study in order to
825 avoid further confusion.

826

Table 1. Peak positions of DB1 and DB2 Raman spectra of olivine recorded in different lithologies of the Taiban meteorite.

Olivine location	DB1 (cm^{-1})	DB2 (cm^{-1})	Fo(%) (Raman)	Fo(%) (EPMA)
Ol in crack	823.8	856.4	93.8	93.6
Ol within ringwoodite	823.4	856.8	87.6	92.1
Ol host rock	820.9	852.4	77.8	75.5

Mg/(Mg+Fe) ratios are calculated both using the Raman calibration developed by Kuebler et al. (2006) and by EPMA. Accuracies of the Raman calculated values are within Fo±10%, and those of the EPMA are within Fo±5%.

Table 2: EPMA analyses of minerals in the Taiban chondrite.

	mtj	cpx	rgt l-bl	rgt cl	rgt bl	rgt cl2	ol crk	ol 1	ol 2	ol 3	ol host
wt%											
SiO_2	52.99	53.87	37.73	37.95	37.38	36.80	40.47	40.63	40.38	40.80	37.35
TiO_2	0.17	0.46	-	0.02	-	-	-	-	-	-	-
Al_2O_3	0.18	0.53	-	0.01	-	0.01	0.06	0.32	0.32	0.13	0.01
Cr_2O_3	0.10	0.77	-	0.18	-	0.07	0.01	0.02	0.02	0.01	0.02
FeO	14.53	4.89	24.82	24.69	25.96	25.28	6.42	8.46	7.47	6.26	22.55
MnO	0.48	0.23	0.11	0.10	0.03	0.06	1.67	2.01	2.04	2.02	0.53
MgO	28.33	16.87	37.17	37.28	36.28	37.12	49.19	48.11	48.37	50.02	38.89
CaO	0.70	21.85	0.05	0.07	0.04	0.02	0.04	0.06	0.07	0.07	0.03
NiO	-	0.04	-	-	0.04	-	0.07	0.25	0.28	0.09	0.02
P_2O_5	0.03	0.02	0.06	0.01	0.08	0.02	0.07	0.01	0.01	0.02	0.03
Na_2O	0.01	0.48	0.01	-	0.01	0.01	-	-	-	-	0.01
Total	97.53	100.02	99.96	100.32	99.85	99.42	97.98	99.88	98.97	99.42	99.44
$Fo_{\%}$			72.75	72.91	71.36	72.35	93.17	91.02	92.02	93.44	75.46
Calculated cations per formula unit											
Si	3.9180	1.9749	0.9934	0.9949	0.9911	0.9793	1.0030	0.9992	0.9985	0.9979	0.9820
Ti	0.0097	0.0126	-	0.0004	-	-	-	-	-	-	-
Al	0.0154	0.0229	-	0.0003	-	0.0003	0.0016	0.0092	0.0093	0.0039	0.0002
Cr	0.0059	0.0223	-	0.0037	-	0.0015	0.0002	0.0003	0.0003	0.0001	0.0005
Fe	0.8986	0.1500	0.5466	0.5414	0.5756	0.5627	0.1331	0.1741	0.1546	0.1280	0.4958
Mn	0.0303	0.0072	0.0025	0.0022	0.0007	0.0014	0.0350	0.0419	0.0428	0.0419	0.0117
Mg	3.1231	0.9218	1.4591	1.4572	1.4340	1.4725	1.8172	1.7639	1.7830	1.8239	1.5244
Ca	0.0552	0.8584	0.0013	0.0020	0.0013	0.0007	0.0010	0.0016	0.0019	0.0018	0.0008
Ni	-	0.0012	-	-	0.0008	-	0.0015	0.0050	0.0056	0.0018	0.0004
P	0.0016	0.0006	0.0014	0.0002	0.0019	0.0004	0.0014	0.0001	0.0003	0.0004	0.0006
Na	0.0019	0.0344	0.0003	-	0.0008	0.0006	-	-	-	-	0.0008
O	12	6	4	4	4	4	4	4	4	4	4

mjt: majorite; cpx: high-Ca pyroxene; rgt l-bl: light blue ringwoodite, rgt cl: colorless ringwoodite, rgt bl: blue ringwoodite, rgt cl2: clear ringwoodite in different crystal. ol crk: olivine in the crack of the studied ringwoodite; ol 1, ol 2, ol 3: three measurements of olivine within the studied ringwoodite crystal; ol host: olivine in the host rock; -: below detection limit.

$Fo_{\%} = [Mg/(Fe+Mg)] \times 100$

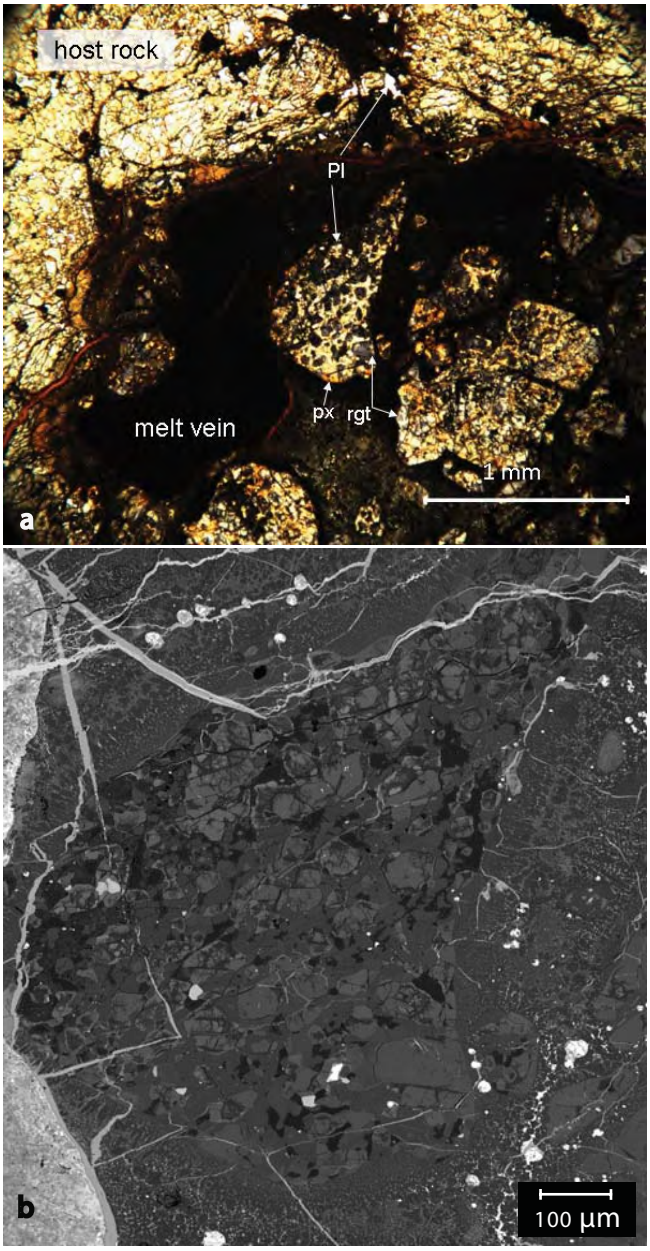

Figure 1

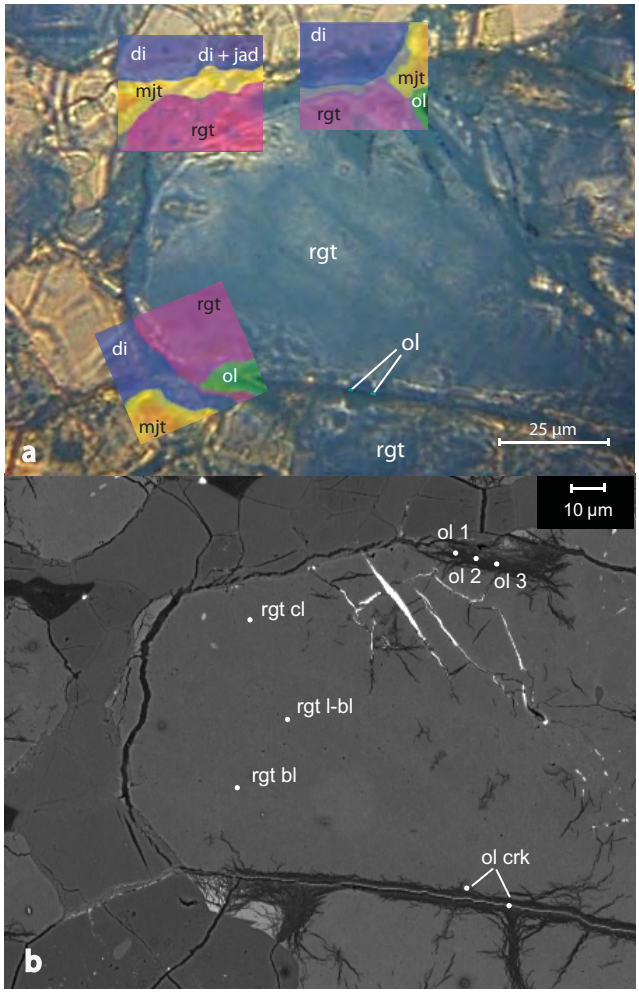
di
di + jad
mjt
rgt
di
mjt
ol
rgt
rgt
rgt
di
ol
mjt
ol
25 µm
a
rgt
10 µm
ol 1
ol 2
ol 3
rgt cl
rgt l-bl
rgt bl
ol crk
b

Figure 2

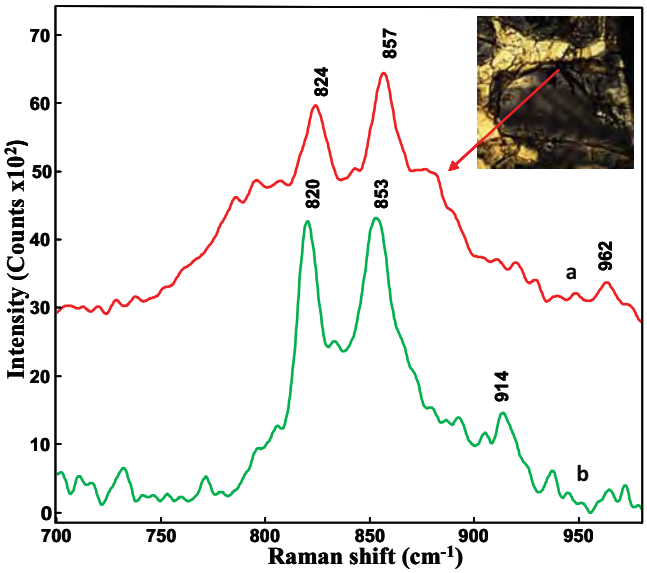
Intensity (Counts x10²)
Raman shift (cm⁻¹)
824
857
820
853
914
962
a
b
0
10
20
30
40
50
60
70
700
750
800
850
900
950

Figure 3

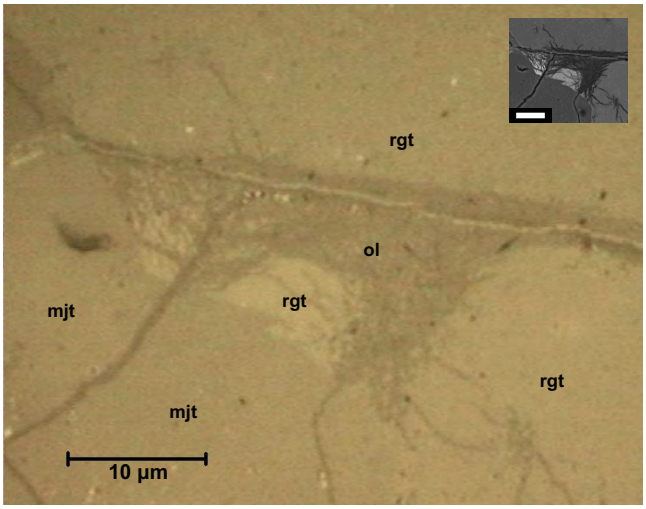

Figure 4

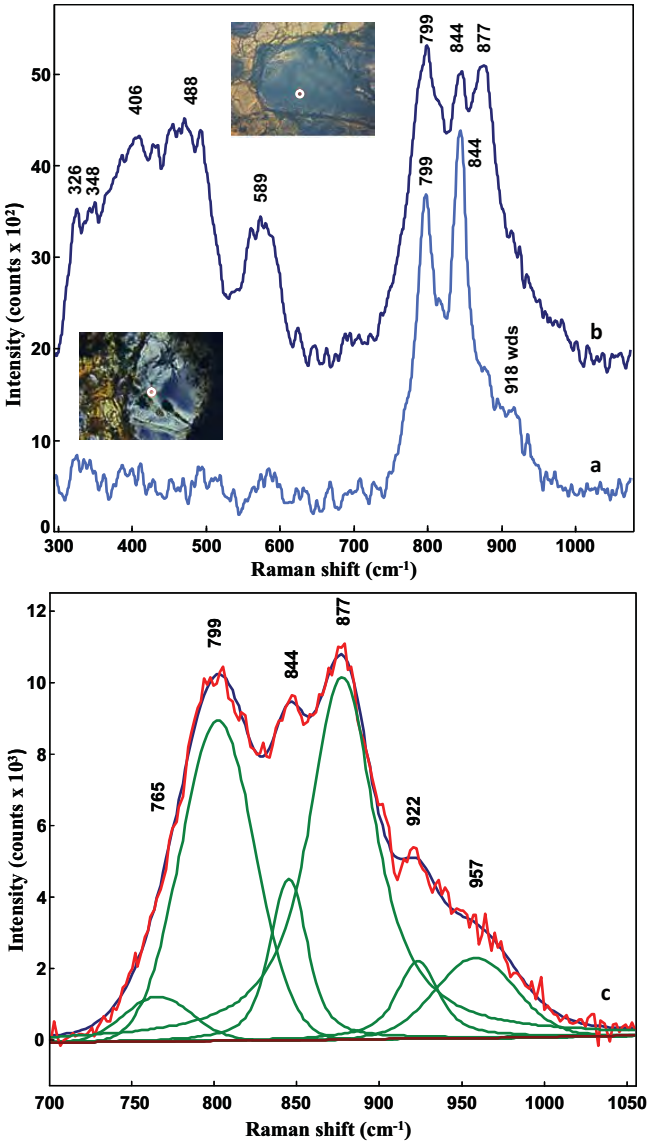
Intensity (counts x 10²)
Raman shift (cm⁻¹)
326
348
406
488
589
799
844
877
799
844
918 wds
b
a
Intensity (counts x 10³)
765
799
844
877
922
957
c

Figure 5

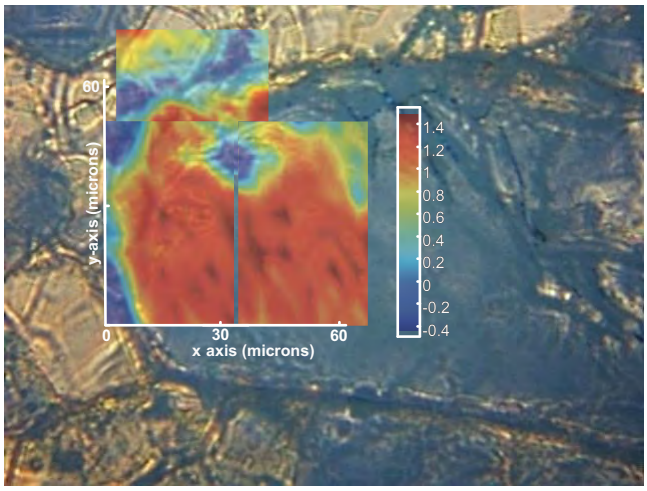

Figure 6

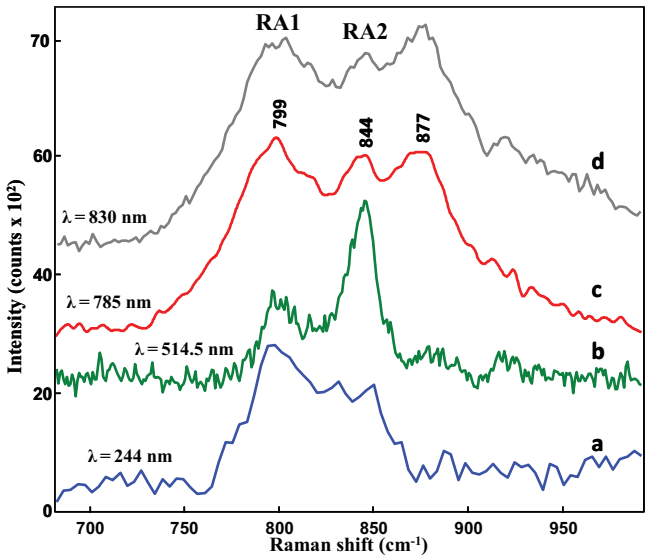
RA1
RA2
799
844
877
d
c
b
a
λ = 830 nm
λ = 785 nm
λ = 514.5 nm
λ = 244 nm
Intensity (counts x 10²)
Raman shift (cm⁻¹)
0
20
40
60
70
700
750
800
850
900
950

Figure 7

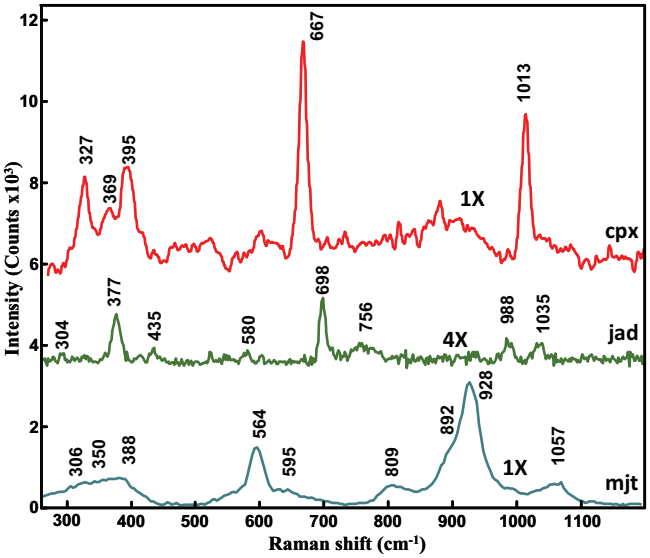
Intensity (Counts x10³)
Raman shift (cm⁻¹)
667
1013
327
369
395
1X
cpx
377
304
435
580
698
756
988
1035
4X
jad
928
892
564
306
350
388
595
809
1057
1X
mjt

Figure 8

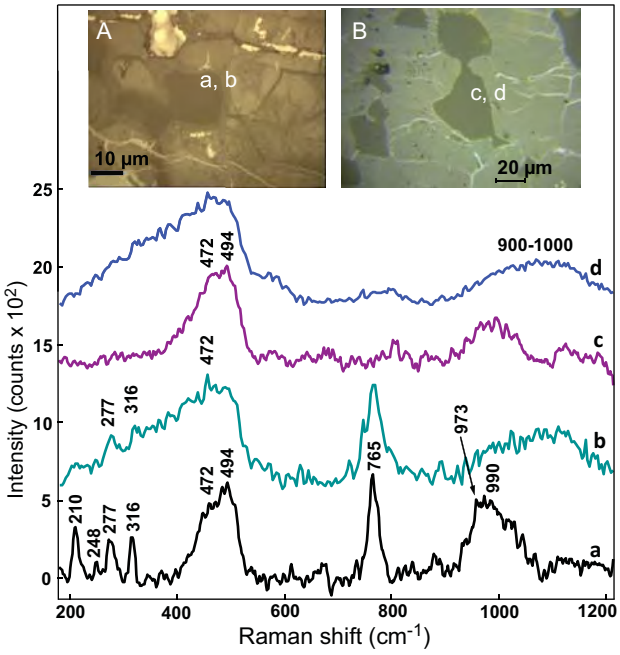
A
a, b
10 μm
B
c, d
20 μm
900-1000
d
c
b
a
472
494
277
316
973
765
990
210
248
Intensity (counts x 10²)
Raman shift (cm⁻¹)
0
5
10
15
20
25
200
400
600
800
1000
1200

Figure 9